ARTICLES
https://doi.org/10.1038/s41928-018-0129-6
nature electronics

Writing monolithic integrated circuits on a two-dimensional semiconductor with a scanning light probe

Seung-Young Seo[1,2], Jaehyun Park[1,2], Jewook Park[1], Kyung Song[3], Soonyoung Cha[4], Sangwan Sim[1], Si-Young Choi[2], Han Woong Yeom[1,5], Hyunyong Choi[4] and Moon-Ho Jo[1,2,5*]

The development of complex electronics based on two-dimensional (2D) materials will require the integration of a large number of 2D devices into circuits. However, a practical method of assembling such devices into integrated circuits remains elusive. Here we show that a scanning visible light probe can be used to directly write electrical circuitry onto the 2D semiconductor molybdenum ditelluride (2H-$MoTe_2$). Laser light illumination over metal patterns deposited onto 2D channels of 2H-$MoTe_2$ can convert the channels from an n-type semiconductor to a p-type semiconductor, by creating adatom–vacancy clusters in the host lattice. With this process, diffusive doping profiles can be controlled at the submicrometre scale and doping concentrations can be tuned, allowing the channel sheet resistance to be varied over four orders of magnitudes. Our doping method can be used to assemble both n- and p-doped channels within the same atomic plane, which allows us to fabricate 2D device arrays of n–p–n (p–n–p) bipolar junction transistor amplifiers and radial p–n photovoltaic cells.

Two-dimensional semiconductors and van der Waals heterostructures composed of layered two-dimensional (2D) semiconductors are promising materials for developing the next generation of electronic and optoelectronic devices[1–6]. However, demonstrations of monolithically integrated circuits based on such semiconductors are limited, despite extensive research on the growth of these materials[7–14]. To fabricate discrete test devices made from individual 2D semiconductors, manual transfer methods[15,16] are usually employed, but these approaches are not scalable. Local doping of the monolithic channels is an alternative strategy, but recent demonstrations have used vapour- or solution-phase dopant precursors that are not site-specific, and instead globally dope the entire channel, and thus offer only limited control over dopant profiles[17–22]. To build practical 2D integrated circuits, a simple doping process is required that can offer local doping of the 2D semiconductor channels and with controlled dopant concentrations, as is typically achieved with ion implantation in silicon complementary metal–oxide–semiconductor (CMOS) processing.

In this Article, we report the writing of integrated circuits on a 2D semiconductor using a visible laser. In particular, by scanning the laser over metal patterns deposited on 2H-$MoTe_2$ semiconductor layers we achieve spatially resolved doping, with controlled dopant profiles and concentrations. This allows us to directly write various circuitry in designed patterns, including arrays of n–p–n (p–n–p) bipolar junction transistors (BJTs) and p–n diode discs. We chose atomically-thin $MoTe_2$ as a model channel system, due to the relative ease of manipulating the bonding in $MoTe_2$ and doping the lattice by creating extrinsic point defects, as compared with MoS_2 and $MoSe_2$.

Light-induced p-doping in metal-patterned $MoTe_2$ layers

Our experimental set-up[23,24] (Fig. 1a,b) uses a focused laser beam (wavelength $\lambda = 532$ nm and power $P_{laser} = \sim 20$ mW) to locally illuminate patterned Au electrodes on pristine 2H-$MoTe_2$ films (thickness = 2.2–20 nm). These 2H-$MoTe_2$ channels were designed to form in various shapes by CF_4 dry-plasma etching with photoresist masks, followed by deposition of electrode arrays (Cr 1 nm/Au 20 nm) to produce multiple channels in a back-gate field-effect transistor (FET) geometry. Thinner 2H-$MoTe_2$ films (<5 nm) were directly grown on SiO_2/p^+-Si substrates by chemical vapour deposition, whereas thicker films (>5 nm) were mechanically exfoliated from single crystals (see Methods). Regardless of the given thickness variation and preparation methods, our pristine $MoTe_2$ films were initially n-type semiconductors (energy bandgap, E_g, of ~1.0 eV), as confirmed with the FET and spectral photocurrent measurements (Supplementary Fig. 1).

The devices in Fig. 1b were selectively laser scanned for 30 seconds along the green dotted lines on the contact electrodes 1 and 2 in atmospheric conditions. Initially pristine (nominally undoped and without light illumination) 2H-$MoTe_2$—that is, the channel that contacts electrodes 3 to 4—displays n-type characteristics, as verified by the output (I–V_b at $V_g = 0$ V) and transfer (I–V_g at $V_b = 0.5$ V) curves (Fig. 1c,d). In contrast, the $MoTe_2$ channel between the illuminated contacts 1 and 2 showed typical p-type characteristics. The channel 1–2 becomes seemingly insulating after light illumination (Fig. 1c). However, it is a direct result of p-doping, as clearly observed in the I–V_g curve with a similar current magnitude (Fig. 1d). At the same time, the I–V_b curve of the channel 2–3 becomes strongly rectifying, indicating the p–n junction is formed therein. The existence of p–n diodes and the E_g of 1.0 eV were analysed with

[1]Center for Artificial Low Dimensional Electronic Systems, Institute for Basic Science (IBS), Pohang, Korea. [2]Department of Materials Science and Engineering, Pohang University of Science and Technology (POSTECH), Pohang, Korea. [3]Department of Materials Modeling and Characterization, Korea Institute of Materials Science, Changwon, Korea. [4]School of Electrical and Electronic Engineering, Yonsei University, Seoul, Korea. [5]Department of Physics, Pohang University of Science and Technology (POSTECH), Pohang, Korea. *e-mail: mhjo@postech.ac.kr

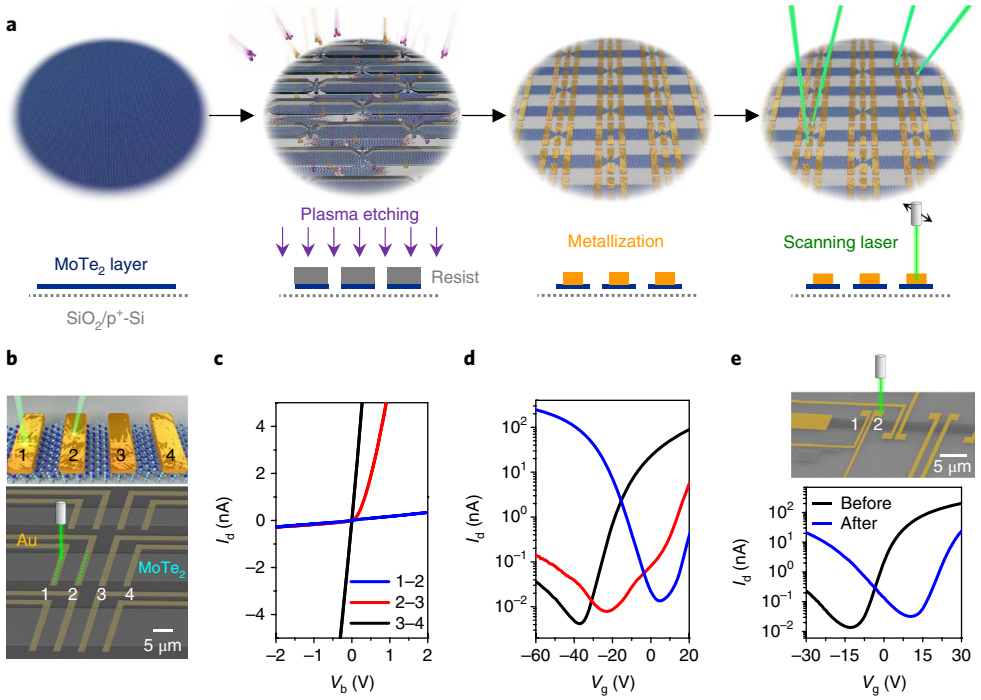

Fig. 1 | Direct writing of electrical circuitry on a single semiconductor layer by scanning a visible laser. a, Schematic of circuit fabrication on a $MoTe_2$ layer by conventional lithography and laser writing. **b**, SEM image of $MoTe_2$ back-gated FET devices. The 532-nm laser illuminated the pair of top-contact metal electrodes 1 and 2. **c**, *I*–*V* characteristics of each channel with pairs of contacts 1–2 (blue line), 2–3 (red line) and 3–4 (black line). **d**, The transfer curve (I–V_g) of each channel on SiO_2/p^+-Si substrates. **e**, SEM image (top) and the transfer curve (bottom) of a $MoTe_2$ FET device with static light illumination 'off' the $MoTe_2$ channels (~2 μm away from the $MoTe_2$ channel edge).

a conventional diode fit and scanning photocurrent imaging and spectroscopy as a function of V_b (Supplementary Fig. 1).

The role of the patterned Au electrodes on the 2H-$MoTe_2$ channels under the illumination conditions (wavelength of 532 nm and optical power approximately 20 mW), in comparison to the cases of direct illumination[25,26], is considered to be as a geometrical guide for the heat that is generated by local light absorption in the visible range in Au because of the much higher thermal conductivity of Au (~300 $W m^{-1} K^{-1}$) compared to that of $MoTe_2$ (~3 $W m^{-1} K^{-1}$). Figure 1e is the case where the static light illumination 'off' the $MoTe_2$ channels (~2 μm away from the $MoTe_2$ channel edge) reproducibly induced a similar doping effect on the channel (see Supplementary Figs. 2–7 for detailed control experiments).

Microscopic mechanism of p-doping

Direct evidence of the apparent *p*-type doping was captured with scanning tunnelling microscopy and spectroscopy (STM/STS) investigations (Fig. 2a; see Methods for further details of STM sample preparation). The STM topography of pristine areas (Fig. 2b), which are sufficiently away (>300 μm) from the illumination spot, showed atomically resolved 2H-$MoTe_2$ lattices, where the bright protrusions correspond to the Te atoms in the Te–Mo–Te trigonal prisms (the inset of Fig. 2b)[27]. The differential conductance (dI/dV) at the pristine lattices, which represents the local density of states (LDOS), showed that the observed energy bandgap is indeed ~1.0 eV and the conduction band minimum (CBM) is near the Fermi level, implying the n-type characteristics of the host lattices (Fig. 2d), consistent with the device characteristics of Fig. 1. In addition, we identified adatom defects (Fig. 2b; assigned as type A defects). These are likely to be physisorbed adatoms (heights ~2 Å), because they can migrate during the tip scanning (Supplementary Fig. 8). These are presumed to be single-atom species, as they invariably exhibited triangular protrusions around the Te sites of the host lattice, and are probably H atoms, which are typically present in ultrahigh vacuum (UHV) conditions. We have also observed individual Te vacancies (Supplementary Fig. 9) as point defects[28,29]. These type A defects and Te vacancies are regarded as intrinsic defects, as they are persistently found regardless of light illumination (Supplementary Fig. 10). The local dI/dV spectrum at the type A defects (the red line in Fig. 2d) shows mid-gap states at $V = -0.6$ V with a down-shifted valence band maximum (VBM). In other words, the type A defects act as electron donors in the host lattices.

We found substantially different defect characteristics near the illuminated area (assigned as type B and C defects). The atomically resolved topography of the type B defect exhibits a notable pit at the Mo site, neighbouring the bright Te atom sites, which implies that the type B defect is a single Mo vacancy (Fig. 2f and Supplementary Fig. 9), as has been similarly observed[30] in WSe_2. Often, it is a chalcogen vacancy, which is naturally occurring as a common defect in transition-metal dichalcogenides (TMDCs). However, in our case, the light-induced heating generates these additional transition-metal point vacancies. Nonetheless, the value of dI/dV at this type B defect site is similar to that of the pristine 2H-$MoTe_2$ (Fig. 2g), suggesting that the type B defect is not an active dopant in our case.

The type C defect appears as a cluster with a large surrounding corrugation (heights ~5–7 Å and radii ~2 nm) with no particular atomic features (Fig. 2h). Interestingly, the LDOS at the type C defect site exhibits a substantial potential shift of ~0.5 eV towards the unoccupied states (Fig. 2i). This finding is also supported by the 2D line spectroscopy across the type C defect, where local variations of the CBM and VBM positions and the band-edge tails are captured at the atomic scale (Fig. 2j). These observations strongly suggest that the type C defect is an electron acceptor in the host $MoTe_2$ lattice. Considering the relatively large size and the shape of the protrusions, the type C defects can be assigned to adatom clusters that are electrically charged, presumably fixed at certain point defects of the host lattice (Supplementary Fig. 8). Recent studies of vapour phase doping on 2D $MoTe_2$ crystals suggested that absorption of

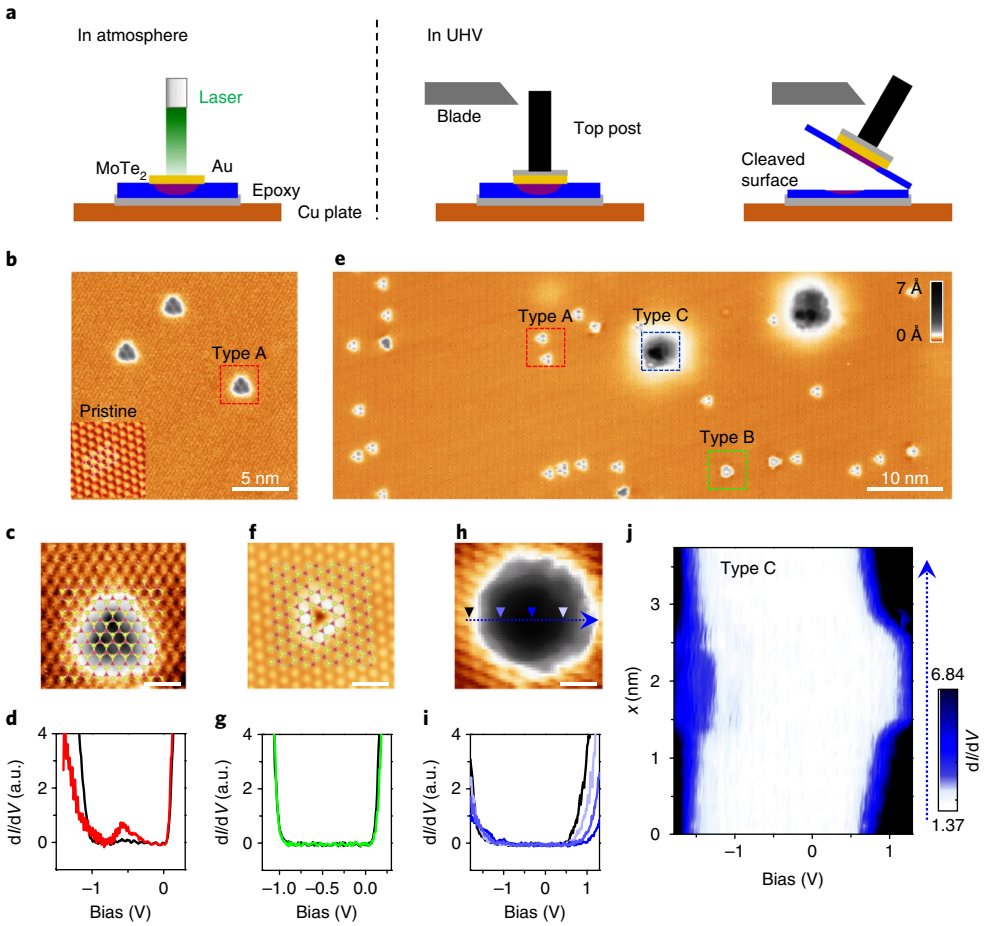

Fig. 2 | Microscopic origin of p-type doping in 2H-$MoTe_2$ upon light illumination. a, Schematic image of sample preparation process for STM/STS of 2H-$MoTe_2$ after light illumination. **b**, STM topography of 2H-$MoTe_2$ at the pristine area ($V = -1.5$ V, $I_{tip} = 200$ pA) (inset) atomically resolved 2H-$MoTe_2$ lattice. **c**, Atomically resolved topography of the type A defect (red square in **b**). **d**, Differential conductance (dI/dV) curves acquired at the pristine $MoTe_2$ (black) and the type A (red) defect centre in **c**. **e**,STM topography near the illumination spot ($V = -1.5$ V, $I_{tip} = 200$ pA). Red, green and blue squares indicate adatom, Mo vacancy and clustered defects, respectively. **f**, Atomically resolved topography ($V = -1.2$ V, $I_{tip} = 200$ pA) of the type B defect (green square in **e**). **g**, Corresponding dI/dV curves acquired at pristine (black) and Mo defect (green) sites in **f**. **h**, Magnified STM topography of the type C defect. **i**, dI/dV curves at the positions marked in colour in **h**. **j**, 2D plot of all dI/dV curves along the dotted arrow in **h**. Amber and grey colour scales in the STM topography images represent $MoTe_2$ lattice and defect protrusion, respectively. Scale bars in **c**, **f** and **h** are 1 nm.

atmospheric oxygens or water molecules is responsible for p-type doping[19–21]. Our atomic-scale observations suggest that these type C defects are oxygen molecules (or more precisely oxygen clusters), diffused into the van der Waals gaps during the light illumination as the major p-dopants, although the exact molecular conformations are yet to be determined. Statistically we count a greater number of type B and type C defects (~10^{11} cm^{-2}) in the region nearer to the light illumination, varying on the order of ~10^{11}–10^{12} cm^{-2} (Supplementary Fig. 10). On the basis of recent density functional theory calculations and experimental observations, it is generally accepted that oxygen acts on TMDCs as a p-dopant[19,31]. It was also reported that the Te vacancy stabilizes the bonded oxygens to $MoTe_2$ lattices[31] and accordingly 0.2 electrons are transferred from 2H-$MoTe_2$ to O_2, resulting in p-doped 2H-$MoTe_2$.

We employed the STM/STS to probe individual dopants at the atomic scale and provide atomic electron structures of individual dopants, although inherently it does not provide information on individual chemical structures. Thus, we performed energy-dispersive X-ray spectroscopy in scanning transmission electron microscopy (STEM) (Supplementary Figure 11) on our $MoTe_2$ crystals (5 nm thick) after direct light illumination on a transmission electron micosopy (TEM) (Cu/Au) grid, and confirmed strongly enhanced oxygen signals near the illumination spot. This observation supports the scenario that local light illumination creates single Mo vacancies, followed by on-site chemical absorption of oxygen clusters, acting as the p-dopants within the channel.

Fast programmable doping

Because the local p-type doping in our study is a result of the light-induced creation of molecule–vacancy clusters within the n-type host lattices, the doping profile can be manipulated with illumination time as a simple process parameter in the circuit fabrication (Fig. 3). First, we performed channel length and thickness dependence measurements (Supplementary Figs. 12 and 13). At a constant illumination time of 60 s, we find that channels below 1 μm length become highly p-doped, suggesting the doping profile can be adjusted on the submicrometre scale. By varying the channel thickness as 12.7, 7.6, 6.2 and 3.2 nm, we observed progressively stronger p-type characteristics with a larger on/off ratio on thinner channels. Apparently our doping process is dependent on the channel length and thickness (Supplementary Fig. 13). We also performed illumination-time-dependent doping with various channel lengths (Fig. 3a) and Hall measurements (Fig. 3b). As seen in Fig. 3c, in the 1.0-μm-long channel, the sheet resistance,

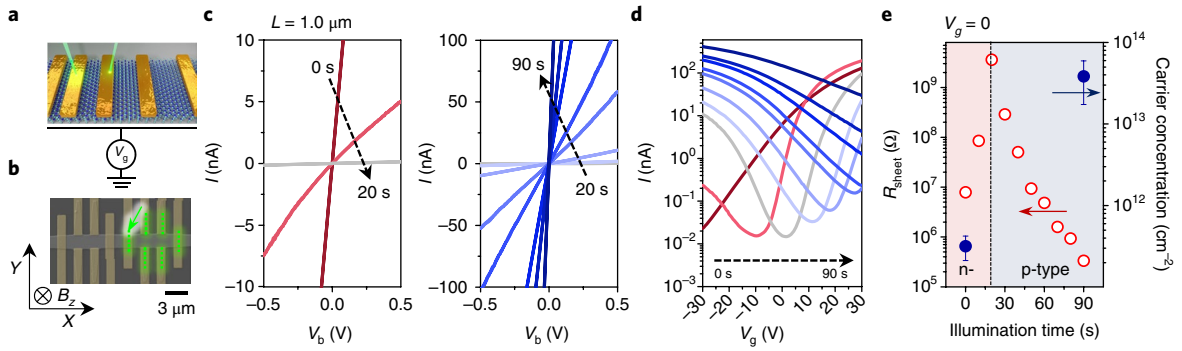

Fig. 3 | Programmable local p-type doping by light illumination. a, Schematic of illumination-time-dependent p-doping on a 1-μm-long $MoTe_2$ channel in a back-gated FET array. **b**, SEM image of Hall bar devices, where a scanning laser illuminated the metal contacts marked by green dashed lines. **c**, *I*–*V* characteristics at laser illumination times from 0 to 90 s in increments of 10 s. **d**, Corresponding transfer curves (I–V_g, at $V_b = 50$ mV). **e**, Variation in the channel sheet resistances and carrier concentrations with illumination times from 0 to 90 s. Error bars show the error range of carrier concentration in Hall measurement.

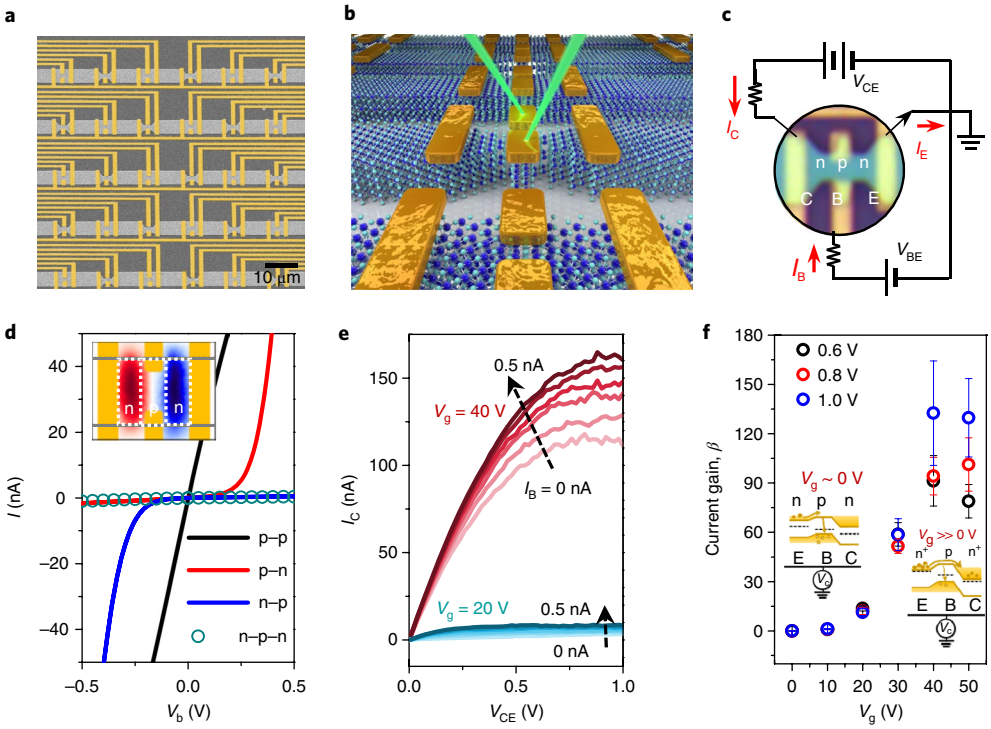

Fig. 4 | Direct writing of integrated bipolar junction transistor arrays. a,**b**, SEM image (**a**) and schematic (**b**) of $MoTe_2$ BJT arrays. **c**, Circuit diagram of the n–p–n BJT in the common emitter (CE) configuration. Local illumination was applied to the inner electrodes along the channels to configure the p-type base (B) terminal, leaving the left and right electrodes to be configured to the n-type collector (C) and emitter (E) terminals. **d**, *I*–*V* characteristics of each channel within the n–p–n BJT. Black line: p-type channel between two electrodes in the base. Red line: p–n channel between the base and emitter. Blue line: n–p channel between the collector and base. Green circles: n–p–n channel between the emitter and collector. Inset: scanning photocurrent imaging of the n–p–n BJT device. **e**, Output characteristics of n–p–n BJT in the common-emitter configuration at $V_g = 20$ V (blue traces) and 40 V (red traces). I_B was varied from 0 to 0.5 nA in increments of 0.1 nA. **f**, V_g-dependent current gain β with $V_{CE} = 0.6$, 0.8 and 1.0 V. Inset: energy band diagrams with small V_g (upper left) and large V_g (lower left). Error bars show the standard deviation of current gain in the range of $0.5\ \text{V} < V_{CE} < 1\ \text{V}$.

R_{sheet}, increased for the first 20 s of illumination (left-hand panel) and then decreased between 20 and 90 s (right-hand panel). This systematic change in R_{sheet} was clearly verified as gradual p-doping in a series of transfer curves (I–V_g at $V = 0.05$ V in Fig. 3d); the channel was n-type before light illumination and was gradually doped to p-type during light illumination, until it became degenerated. The corresponding values of R_{sheet} varied over four orders of magnitudes from 0.2 MΩ to 3 GΩ (Fig. 3e). This was also verified by Hall measurements: the initial carrier (electron) concentration before light illumination was 2.5×10^{11} cm^{-2} and the highest hole concentration of 3.0×10^{13} cm^{-2} was reached after 90 s of illumination. The overall observations demonstrate that local doping can be precisely programmed by means of the illumination time within a minute over the submicrometre length scale. In regard to the reproducibility of our doping process, we tested more than 40 FET devices to obtain the statistical variation of FET mobility and

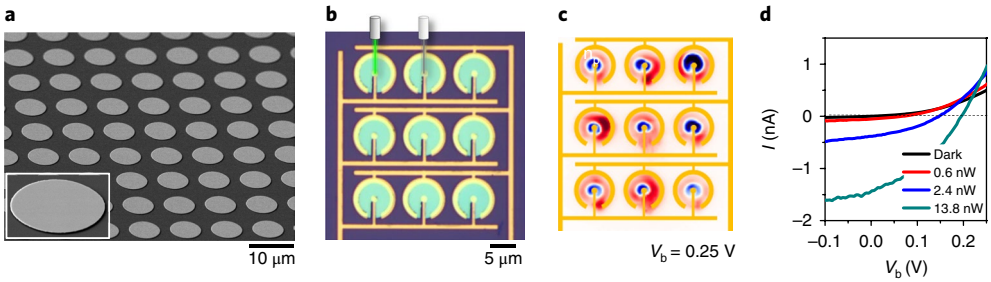

Fig. 5 | Circularly patterned coplanar $MoTe_2$ p–n junction arrays as photovoltaic cells. a, SEM image of circular pattern arrays. **b**, Optical image of circular p–n diode arrays, where the laser illuminated the centre electrodes. **c**, Scanning photocurrent image of the p–n diode with $V_b = 0.25$ V. **d**, Photovoltaic responses (I_{ph}–V curves) of the p–n diode under a 1,200-nm excitation laser at optical powers of 0 (black line), 0.6 nW (red), 2.4 nW (blue) and 13.8 nW (green).

found stable device performances before and after light illumination (Supplementary Fig. 14).

Writing fabrication of coplanar BJTs and photovoltaic cells

Local light-induced p-doping within the *n*-$MoTe_2$ channels enables direct writing of individual circuit elements and their integration into 2D coplanar circuitry. As a proof of concept, we directly wrote arrays of n–p–n bipolar junction transistors (BJTs) within a patterned $MoTe_2$ layer on SiO_2/p$^+$-Si substrates (Fig. 4a,b); we also created a p–n–p BJT with the common-base configuration (Supplementary Fig. 15). Figure 4c shows an n–p–n BJT, configured to a common-emitter geometry as a current amplifier. Local p-doping was achieved by selective illumination for 30 s on the inner electrodes along the 4-μm-long channels to configure the p-type base (B) terminal, and on the left and right electrodes to configure the n-type collector (C) and emitter (E) terminals. Here, the common-emitter current gain is defined as $\beta = (I_C - I_{C0})/I_B$, where I_{C0} is the reverse saturation current at the base–collector junction (see Supplementary Fig. 16 for the output characteristics in the common-base configuration). Scanning photocurrent (I_{ph}) imaging of the device visually verified that two p–n diodes are connected back-to-back to form an n–p–n BJT (the inset of Fig. 4d). Diode I–V characteristics verify that the base–collector junction is p–n (red) and the emitter–base junction is n–p (blue) in Fig. 4d. In the output characteristics (I_C–V_{CB}), the output collector current, I_C, was amplified in the range 3–9 nA with a small input current, I_B, of 0.5 nA, where β was measured to be relatively small (approximately 10–20; Fig. 4e, lower blue traces). Because our n–p–n BJT is placed on SiO_2/p$^+$-Si substrates, the energy offsets within the BJT (and thus the doping profiles at the emitter, base and collector regions and the depletion widths at the emitter–base and base–collector junctions) can be further tuned by applying a positive back-gate voltage, V_g; the device thereby becomes converted to an n$^+$–p–n$^+$ BJT. Indeed, applying $V_g > 40$ V substantially increases β to >150 (Fig. 4f). As illustrated in the insets, the heavy doping of the emitter and collector increases the injection efficiency (that is, the ratio of carriers injected by the emitter to those injected by the base). The heavy doping of the emitter region and light doping of the base region causes substantially more electrons to be injected into the base than holes to be injected from the base into the emitter.

Writable doping can also be employed to design coplanar device architectures in arbitrary shapes. We patterned an array of circular $MoTe_2$ over a large area and configured each electrode on the centre and periphery of the circle by lithography. Translational shots of light illumination for 1 min per single shot on the centre electrodes in the array yielded an array of disc-shaped (or Corbino disc) p–n diodes (Fig. 5a,b), where the unwanted edge leakage current is geometrically prohibited[32]. Scanning photocurrent imaging on the ring (Fig. 5c) confirmed that the radial junctions were p–n junctions, similar to Fig. 1c. We then examined the photovoltaic response of the disc diodes by global illumination with various incident optical powers of a 1,200 nm laser. In Fig. 5d, the black line is the dark I–V curve, and the red, blue and green lines correspond to the photovoltaic I–V curves with 0.6, 2.4 and 13.8 nW optical powers, clearly demonstrating the photovoltaic operation. We measured the external quantum efficiency (EQE), defined as the ratio of the number of charge carriers collected to the number of photons, $EQE = (I_{ph}/e)/(P_{opt}/h\nu)$, where I_{ph} is the photocurrent at $V_b = 0$, e is the elementary charge, P_{opt} is the optical power, h is the Planck constant, and ν is the light frequency, and obtained EQE values of approximately 10, 16 and 11% with optical powers of 0.6, 2.4 and 13.8 nW, respectively. This value is one order of magnitude higher than that obtained using MoS_2 or WSe_2 intra-monolayer p–n photovoltaic cells[33,34] and comparable to that of high-performance 2D TMDC/graphene vertical-stack photopoltaic cells[35].

Conclusions

We have reported the fabrication of integrated circuits on atomically-thin 2H-$MoTe_2$ semiconductor channels. Using a self-aligned doping approach with a scanning visible light probe, we demonstrated programmable writing of various 2D circuits in which both n- and p-doped channels are assembled within the same atomic plane. Our programmable doping method is quick, simple and offers a high level of accuracy. Our approach could be of value in the development of massively parallel circuitry based on 2D semiconductors.

Methods

Preparation and synthesis of 2H-$MoTe_2$ crystals. Our few-layer 2H-$MoTe_2$ crystals were grown by vapour transport synthesis from solid powder precursors at 650–670 °C. A mixture of MoO_3 (99.5 %) and NaCl (≥ 99.8 %) was placed in an alumina boat with SiO_2 (300 nm)/Si wafers. Tellurium (≥ 99.5 %) powder was placed away from the centre of the tube furnace (diameter 3.81 cm, length 30.48 cm) to supply Te vapour continuously along the tube furnace. Bulk 2H-$MoTe_2$ crystals, which we exfoliated for device fabrications, were commercially purchased from '2D Semiconductors' with the specification 'undoped (intrinsic semiconductor), purity: 99.9999% confirmed and defect concentration ~10^{12} cm^{-2}'.

STM sample preparation. The samples for STM analysis were prepared (Fig. 2a) by first using the focused laser to illuminate the top electrodes on pristine 2H-$MoTe_2$ in atmospheric conditions, and then transferring the samples to the UHV STM chamber. The crystal was then cleaved in the STM load-lock chamber (base pressure $<1\times10^{-7}$ torr), and the STM investigation was performed in the main UHV chamber (78 K at $<1\times10^{-10}$ torr). The illuminated areas were easily distinguished from the pristine $MoTe_2$ areas by means of long-working-distance optical microscopy. We note that the STM/STS study was performed on a newly exposed interface following cleaving of the surface, and thus represents the '2D bulk' doping process, rather than solely surface doping.

Electron microscopy investigation. Atomic structures of our 2H-$MoTe_2$ crystals were characterized using a STEM (JEOL JEM-2100F) equipped with an aberration corrector (CEOS). The probe diameter of the beam under an acceleration voltage

of 200 kV was ~0.9 Å. For high-angle annular dark-field (HAADF)-STEM imaging, a probe convergence angle of ~22 mrad was used, and the inner and outer angles of the HAADF detectors were 90 and 200 mrad, respectively. The obtained HAADF-STEM images were bandpass-filtered (HREM Research) to reduce background noise.

Data availability

The data that support the findings of this study are available from the corresponding author upon reasonable request.

Received: 1 April 2018; Accepted: 13 August 2018;
Published online: 13 September 2018

References

1. Britnell, L. et al. Strong light–matter interactions in heterostructures of atomically thin films. *Science* **340**, 1311–1314 (2013).
2. Lee, C.-H. et al. Atomically thin p–n junctions with van der Waals heterointerfaces. *Nat. Nanotech.* **9**, 676–681 (2014).
3. Kappera, R. et al. Phase-engineered low-resistance contacts for ultrathin MoS_2 transistors. *Nat. Mater.* **13**, 1128–1134 (2014).
4. Heo, H. et al. Interlayer orientation-dependent light absorption and emission in monolayer semiconductor stacks. *Nat. Commun.* **6**, 7372 (2015).
5. Cha, S. et al. 1*s* intraexcitonic dynamics in monolayer MoS_2 probed by ultrafast mid-infrared spectroscopy. *Nat. Commun.* **7**, 10768 (2016).
6. Lee, M.-J. et al. Thermoelectric materials by utilizing two-dimensional materials with negative correlation between electrical and thermal conductivity. *Nat. Commun.* **7**, 12011 (2016).
7. Geim, A. K. & Grigorieva, I. V. Van der Waals heterostructure. *Nature* **499**, 419–425 (2013).
8. van der Zande, A. M. et al. Grains and grain boundaries in highly crystalline monolayer molybdenum disulphide. *Nat. Mater.* **12**, 554–561 (2013).
9. Li, M.-Y. et al. Epitaxial growth of a monolayer WSe_2–MoS_2 lateral p–n junction with an atomically sharp interface. *Science* **349**, 524–528 (2015).
10. Kang, K. et al. High-mobility three-atom-thick semiconducting films with wafer scale homogeneity. *Nature* **520**, 656–660 (2015).
11. Zhao, M. et al. Large-scale chemical assembly of atomically thin transistors and circuits. *Nat. Nanotech.* **11**, 954–959 (2016).
12. Liu, L. et al. Heteroepitaxial growth of two-dimensional hexagonal boron nitride template by graphene edge. *Science* **343**, 163–167 (2014).
13. Gong, Y. et al. Vertical and in-plane heterostructures from WS_2/MoS_2 monolayer. *Nat. Mater.* **13**, 1135–1142 (2014).
14. Heo, H. et al. Rotation-misfit-free heteroepitaxial stacking and stitching growth of hexagonal transition-metal dichalcogenide monolayers by nucleation kinetics controls. *Adv. Mater.* **27**, 3803–3810 (2015).
15. Radisavljevic, B., Radenovic, A., Brivio, J., Giacometti, V. & Kis, A. Single-layer MoS_2 transistors. *Nat. Nanotech.* **6**, 147–150 (2011).
16. Britnell, L. et al. Field-effect tunneling transistor based on vertical graphene heterostructures. *Science* **335**, 947–950 (2012).
17. Fang, H. et al. Degenerate n-doping of few-layer transition metal dichalcogenides by potassium. *Nano. Lett.* **13**, 1991–1995 (2013).
18. Yang, L. et al. Chloride molecular doping technique on 2D materials: WS_2 and MoS_2. *Nano. Lett.* **14**, 6275–6280 (2014).
19. Wang, S., Zhao, W., Giustinianoa, F. & Eda, G. Effect of oxygen and ozone on p-type doping of ultra-thin WSe_2 and $MoSe_2$ field effect transistors. *Phys. Chem. Chem. Phys.* **18**, 4304–4309 (2016).
20. Tongay, S. et al. Broad-range modulation of light emission in two-dimensional semiconductors by molecular physisorption gating. *Nano. Lett.* **13**, 2831–2836 (2013).
21. Qu, D. et al. Carrier-type modulation and mobility improvement of thin $MoTe_2$. *Adv. Mater.* **29**, 1606433 (2017).
22. Chang, Y. M., et al, Reversible and precisely controllable p/n-type doping of $MoTe_2$ transistors through electrothermal doping. *Adv. Mater.* **30**, 1706995 (2018).
23. Sung, J. H. et al. Atomic layer-by-layer thermoelectric conversion in topological insulator bismuth/antimony tellurides. *Nano. Lett.* **14**, 4030–4035 (2014).
24. Sung, J. H. et al. Coplanar semiconductor–metal circuitry defined on few-layer $MoTe_2$ via polymorphic heteroepitaxy. *Nat. Nanotech.* **12**, 1064–1070 (2017).
25. Cho, S. et al. Phase patterning for ohmic homojunction contact in $MoTe_2$. *Science* **349**, 625–628 (2015).
26. Parzinger, E., Hetzl, M., Wurstbauer, U. & Holleitner, A. W. Contact morphology and revisited photocurrent dynamics in monolayer MoS_2. *npj 2D Mater. Appl.* **1**, 40 (2017).
27. Hla, S. W., Marinković, V., Prodan, A. & Muševič, I. STM/AFM investigations of β-$MoTe_2$, α-$MoTe_2$ and WTe_2. *Surface Sci.* **352-354**, 105–111 (1996).
28. Hong, J. et al. Exploring atomic defects in molybdenum disulphide monolayers. *Nature Commun.* **6**, 6293 (2015).
29. Liu, X., Balla, I., Bergeron, H. & Hersam, M. C. Point defects and grain boundaries in rotationally commensurate MoS_2 on epitaxial graphene. *J. Phys. Chem. C* **120**, 20798–20805 (2016).
30. Zhang, S. et al. Defect structure of localized excitons in a WSe_2 monolayer. *Phys. Rev. Lett.* **119**, 046101 (2017).
31. Bin, C. et al. Environmental changes in $MoTe_2$ excitonic dynamics by defects-activated molecular interaction. *ACS Nano* **9**, 5326–5332 (2015).
32. Kleinman, D. A. & Schawlow, A. L. Corbino disk. *J. Appl. Phys.* **31**, 2176 (1960).
33. Posposchill, A., Furchi, M. M. & Mueller, T. Solar-energy conversion and light emission in an atomic monolayer p–n diode. *Nat. Nanotech.* **9**, 257–261 (2014).
34. Baugher, B. W. H., Churchill, H. O. H., Yang, Y. & Jarillo-Herrero, P. Optoelectronic devices based on electrically tunable p–n diodes in a monolayer dichalcogenide. *Nat. Mater.* **9**, 262–267 (2014).
35. Lee, C. et al. Atomically thin p–n junction with van der Waals heterointerfaces. *Nat. Nanotech.* **10**, 676–681 (2014).

Acknowledgements

This work was supported by the Institute for Basic Science (IBS), Korea under Project Code IBS-R014-G1-2018-A1. S.C. and H.C. were supported by the National Research Foundation of Korea (NRF) (NRF-2015R1A2A1A10052520 and NRF-2016R1A4A1012929). S.-Y.C. was supported by the Global Frontier Hybrid Interface Materials (GFHIM) of the NRF of Korea (2013M3A6B1078872). K.S. acknowledges the Fundamental Research Program of the Korean Institute of Materials Science.

Author contributions

M.-H.J. and S.-Y.S. conceived and designed the project. S.-Y.S. fabricated the devices and performed light-induced doping experiments, as well as electrical characterizations. Jaehyun P. and Jewook P. performed the STM measurements and analysed the data. H.W.Y. provided the STM set-ups. K.S. and S.-Y.C. acquired the STEM images and analysed the data. S.C., S.S. and H.C. carried out the photocurrent measurements. M.-H.J., S.-Y.S. and Jewook P. co-wrote the paper. All authors discussed the results and commented on the manuscript.

Competing interests

The authors declare no competing interests

Additional information

Supplementary information is available for this paper at https://doi.org/10.1038/s41928-018-0129-6.

Reprints and permissions information is available at www.nature.com/reprints.

Correspondence and requests for materials should be addressed to M.-H.J.

Publisher's note: Springer Nature remains neutral with regard to jurisdictional claims in published maps and institutional affiliations.